processes

MDPI

Article

Multiscale Damage Mechanisms and Long-Term Creep Behavior of Carnallitite

He Wang [1,2,3,*], Xiushan Qin [1,3], Zhixiu Wang [1,3], Hui Wang [1,3] and Lu Chen [1,3]

[1] BGRIMM Technology Group, Beijing 102628, China; qinxiushan@bgrimm.com (X.Q.); wangzhixiu@bgrimm.com (Z.W.); wanghui1@bgrimm.com (H.W.); chenlu@bgrimm.com (L.C.)
[2] School of Resources and Safety Engineering, University of Science and Technology Beijing, Beijing 100083, China
[3] National Centre for International Research on Green Metal Mining, Beijing 102628, China
* Correspondence: 13811118946@126.com

Abstract

To elucidate the mechanisms responsible for the low strength, pronounced variability, and long-term deformation of carnallitite, and to provide a basis for stope parameter design in deep potash mines, two carnallitite seams from a potash mine were investigated. Group C carnallitite and Group D halite-dominated rock salt were subjected to short-term compression tests and multiscale comparative analyses, while Groups A and B carnallitite specimens were tested under multistage creep loading. Particle Flow Code (PFC) simulations were conducted to evaluate the influence of particle size distribution. The results indicate the following: (1) The representative Group C specimens exhibited an average uniaxial compressive strength of 7.83 MPa, which was substantially lower than that of Group D. The acoustic emission (AE), scanning electron microscopy (SEM), and computed tomography (CT) analyses revealed greater heterogeneity in damage evolution and failure behavior, mainly associated with polymineralic composition, weak particle–matrix interfaces, local pores, and insufficient particle connectivity. (2) Particle-scale heterogeneity influenced the load-bearing capacity of carnallitite. In the PFC sensitivity analysis, narrowing the prescribed particle-size-distribution range from 0.4–8.0 mm to 4.0–4.0 mm at a mean particle size of 4.0 mm was associated with an increase in simulated strength from 7.82 to 10.40 MPa. Because quantitative contact-network descriptors were not extracted, the corresponding contact-network interpretation is treated as mechanistic rather than direct quantitative evidence. (3) The long-term uniaxial strengths of Groups A and B were estimated as 3.3 MPa and 4.8 MPa, respectively, using the adopted specific-failure-energy method. The modified Burgers model provided a good fit to the creep data within the tested stress levels, yielding coefficients of determination of 0.957 and 0.964 and root-mean-square error (RMSE) values of 0.0803 and 0.0552 percentage points. Based on the long-term strength constraints and the site-specific design assumptions adopted in this study, the calculated inter-room pillar widths were 6 m for Group A and 4 m for Group B. These findings provide insights into the multiscale damage mechanisms and long-term stability assessment of carnallitite stopes in deep potash mines.

Keywords: carnallitite; particle–matrix weak interface; heterogeneous damage; creep behavior; stress-relief mining

Academic Editor: Qingbang Meng

Received: 24 July 2026
Revised: 14 August 2026
Accepted: 17 August 2026
Published: 18 August 2026

1. Introduction

Potash resources are essential raw materials for agricultural production and the chemical industry. In the underground mining of solid potash deposits, the stability of the surrounding rock, the long-term load-bearing capacity of pillars, and the rationality of stope structural parameters directly affect mine safety and resource recovery. Compared to conventional hard rocks, halite-dominated rock salt, carnallitite, and associated evaporite minerals typically exhibit low strength, pronounced rheology, high susceptibility to damage, and significant heterogeneity. Consequently, the deformation and instability of the surrounding rock exhibit distinct time dependence and structural sensitivity. Previous studies have demonstrated that halite-dominated rock salt undergoes substantial plastic and time-dependent deformation under uniaxial compression and creep loading, indicating that its short-term strength does not directly correlate with its long-term deformation behavior. Sustained creep may occur even at relatively low stress levels, while the steady-state strain rate, damage evolution, and constitutive parameters all influence predictions of long-term stability [1–4]. Therefore, with increasing mining depth and intensified excavation disturbances, strength degradation, creep deformation, and localized damage evolution in weak evaporitic rocks, such as carnallitite, may increasingly compromise the stability of pillars, roofs, and the overall stope.

In recent years, the long-term mechanical behavior and engineering stability of halite-dominated rock salt have been extensively investigated through laboratory testing, long-term predictions, cyclic disturbances, unloading responses, acoustic emission monitoring, and computed-tomography-based damage identification. These studies indicate that transferring laboratory-scale mechanical results to long-term engineering predictions necessitates consideration of time effects, cyclic loading, unloading paths, and cumulative damage. Acoustic emission (AE) and computed tomography (CT) further elucidate damage development from the perspectives of crack activity and internal structural evolution, respectively [5–9]. Laboratory experiments and phenomenological observations have also demonstrated that the creep behavior of rock salt is significantly influenced by crystal orientation, temperature, deviatoric stress, and confining pressure [10,11]. While these studies provide a crucial foundation for understanding the long-term mechanics of evaporitic rocks, most have concentrated on rock salt. The comparatively low strength, pronounced variability, and complex failure characteristics of carnallitite, a strongly heterogeneous polymineralic evaporitic rock, warrant further comparative investigation.

The mechanical behavior of carnallitite is influenced not only by the macroscopic stress level and loading path, but also by factors such as mineral composition, crystal size, particle connectivity, particle–matrix contact relationships, and the development of microcracks. Previous studies have demonstrated that different evaporite mineral assemblages can yield significantly different rheological responses. Furthermore, the presence of impurity minerals, the content of second-phase materials, crystal interfaces, and microfabric can alter the strength, deformation, and creep mechanisms of evaporitic rocks [12–14]. In addition to mineral composition, particle size distribution plays a crucial role in determining macroscopic mechanical behavior. Microstructure-based multiscale approaches have been employed to investigate the impact of grain size distribution on the macromechanical properties of rock salt [15]. The engineering mechanical properties of evaporitic rocks are jointly determined by mineralogy, microstructure, and geological origin, with differences in microfabric leading to substantial variability in mechanical parameters [16–18]. Therefore, an assessment of carnallitite stability based solely on macroscopic strength parameters is insufficient to explain its low strength, significant variability, and long-term deformation.

With advances in microstructural testing techniques, such as CT scanning, scanning electron microscopy (SEM), nuclear magnetic resonance (NMR), and multiscale image

https://doi.org/10.3390/pr14162631

analysis, there has been an increasing application of these methods for internal structure identification and damage mechanism analysis in evaporitic rocks. Multisource microstructural characterization can elucidate damage-induced structural changes associated with pores, cracks, mineral interfaces, and fluid effects. CT scanning, in particular, is effective in identifying the evolution of pores, fractures, and damage during the cyclic fatigue of rock salt [19,20]. For carnallitite, three-dimensional CT reconstruction allows for the characterization of the spatial distribution of particles and the matrix, while SEM provides insights into crystal surface morphology, microcrack development, and compositional differences. The integration of comparative tests on halite-dominated rock salt with macroscopic mechanical tests and CT/SEM characterization of carnallitite establishes connections among their mechanical differences, crystal size, particle connectivity, and particle–matrix interfacial characteristics.

From an engineering perspective, the short-term strength, long-term creep, and structural heterogeneity of evaporitic rocks significantly influence the stability of underground stope structures. Research on energy-storage caverns in bedded salt, as well as the stability and design criteria for such caverns, has demonstrated that stratigraphic structure, surrounding rock conditions, and resource-utilization strategies profoundly affect the long-term stability and economic performance of underground spaces [21–23]. While these studies primarily focus on energy or gas-storage caverns, their insights regarding long-term deformation, structural control, and stability assessment are also pertinent to the design of stopes in deep potash mines. In carnallitite stopes, low strength, pronounced creep, and microstructural heterogeneity can lead to local stress concentrations, sustained pillar deformation, and diminished roof stability. Thus, it is essential to translate multiscale mechanical observations into a framework for stress-relief mining design and structural-parameter determination. Particle flow methods conceptualize rock as a discontinuous medium comprising particles and their interactions, simulating microstructural damage through particle contact, bond breakage, and crack propagation. These methods effectively elucidate how particle-scale structures govern the macroscopic strength and fracture behavior of carnallitite [24,25].

While previous studies provide an important basis for understanding evaporitic-rock mechanics, comparatively fewer studies have integrated the short-term heterogeneous failure of carnallitite with multiscale structural characterization, particle-scale sensitivity analysis, long-term creep response, and site-specific engineering-parameter interpretation within a single framework. The present study therefore treats these components as complementary lines of evidence and explicitly distinguishes direct experimental observations from mechanism-based inference.

In summary, although substantial progress has been made in the mechanical characterization, damage evolution, and engineering stability of evaporitic rocks, several issues concerning carnallitite remain insufficiently resolved. First, the combined effects of mineral assemblage, crystal and particle scale, particle connectivity, and particle–matrix interfaces on its short-term compressive response and heterogeneous damage evolution require further clarification. Second, the long-term creep behavior of carnallitite and its implications for stress-relief mining design remain insufficiently characterized, while the extent to which microstructural features identified from complementary specimens can inform interpretation of time-dependent deformation also requires careful qualification. To address these issues, two carnallitite seams in a potash mine were investigated using uniaxial compression testing, AE monitoring, three-dimensional CT reconstruction, SEM characterization, Particle Flow Code (PFC) simulation, and creep constitutive analysis, with halite-dominated rock salt serving as a reference material. The study integrates short-term mechanical comparison, multiscale characterization, particle-size sensitivity analysis, creep testing, and site-specific stope-parameter interpretation, while avoiding direct cross-group causal inference where the specimen sets are not identical.

2. Materials and Methods

This section delineates the sources of specimens, the unified grouping scheme, and the research program. The investigation comprised two interconnected experimental routes utilizing different batches of specimens. Group C, consisting of carnallitite, and Group D, composed of halite-dominated rock salt, were employed for short-term compression tests and multiscale comparisons. In contrast, Group A and Group B, which comprised carnallitite specimens, were utilized for multistage creep testing, long-term strength evaluation, and the analysis of constitutive parameters. Additionally, PFC simulations were conducted to examine the effects of particle size distribution.

2.1. Specimen Sources

Carnallitite specimens were collected from two seams within a carnallitite deposit, and halite-dominated rock salt, primarily composed of halite (NaCl), was selected as the reference material. Representative cores from the two carnallitite seams were tested to compare their long-term mechanical behavior.

The recovered carnallitite cores had a diameter of 70 mm and were subsequently machined to the dimensions required for the respective tests. To ensure consistent presentation throughout the paper, the carnallitite specimens from the two seams are designated as Groups A and B. The detailed grouping, specimen identifiers, and test purposes are described in Section 2.2. Representative specimens from Groups A and B, before and after loading, are illustrated in Figure 1.

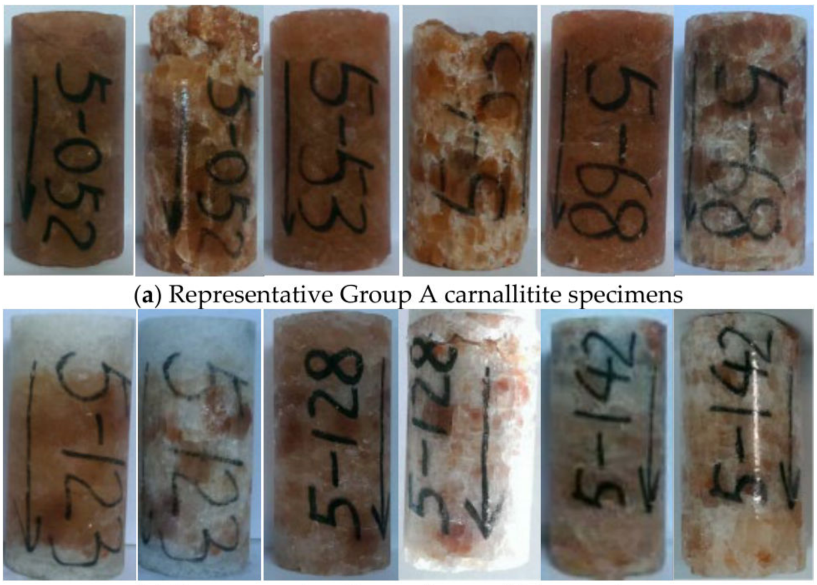

(**a**) Representative Group A carnallitite specimens

(**b**) Representative Group B carnallitite specimens

Figure 1. Representative Group A and B carnallitite specimens before and after loading.

Carnallitite and halite-dominated rock salt are both classified as evaporitic rocks; however, they exhibit distinct differences in their principal mineral assemblages and internal structures. The rock salt is predominantly composed of halite and demonstrates relatively continuous crystal contacts. In contrast, carnallitite contains potassium- and magnesium-chloride phases, along with varying proportions of other evaporite minerals, particle boundaries, and particle–matrix interfaces. Reference rock-salt specimens were included in this study to identify the unique short-term compressive strength, AE response, and microfailure characteristics of carnallitite.

2.2. Experimental Scheme

Due to the varying objectives and stages of the tests, which included long-term mechanical evaluation, short-term compression comparison, and multiscale structural characterization, the specimens were categorized into Groups A, B, C, and D based on their source, test batch, and research purpose. Each specimen was identified with a group letter followed by a sequential number within that group.

Groups A and B consist of carnallitite specimens extracted from the IV-2 and III-11 seams, respectively, serving as the comparative set for long-term mechanical behavior. These specimens were primarily utilized for multistage creep testing, long-term strength estimation, inversion of creep constitutive parameters, and analysis of stope structural parameters. Group C includes specimens selected from the III-11 carnallitite seam, corresponding to the same seam represented by Group B, but from a different experimental batch. These specimens were employed for uniaxial compression testing, AE monitoring, three-dimensional CT reconstruction, and SEM observation, and they also provided experimental data for the calibration of the particle-flow model. Therefore, Group C represents a task-specific characterization set and does not correspond to a third seam or type of carnallitite independent of Groups A and B. Group D consists of halite-dominated rock-salt reference specimens, which were used to compare uniaxial compression responses, AE activity, and SEM microstructure with those of Group C. The labels A-D are utilized exclusively for specimen management and uniform presentation, and they do not indicate lithological types or material grades. The unified identifiers and principal purposes of each group are detailed in Table 1.

Table 1. Specimen groups and principal test purposes.

Specimen Group	Unified Identifiers	Principal Test Purposes
Group A carnallitite	A-1, A-2, A-3, A-4, A-5	Creep testing, long-term strength estimation, inversion of creep constitutive parameters, and stope structural-parameter analysis
Group B carnallitite	B-1, B-2, B-3, B-4, B-5	
Group C carnallitite	C-1, C-2, C-3, C-4, C-5	Uniaxial compression, AE monitoring, CT scanning, SEM characterization, and PFC-model calibration
Group D halite-dominated rock salt	D-1, D-2, D-3, D-4	Uniaxial compression, AE monitoring, and comparative SEM characterization

Note: The listed purposes refer to the overall research tasks assigned to each group and do not imply that every specimen underwent all tests. Individual specimens were allocated to specific tests or analyses according to the experimental program.

Because Groups A/B and C/D were obtained from different experimental batches and were prepared for different test objectives, direct quantitative comparison across the two experimental routes is not intended. The short-term mechanical and microstructural results from Groups C and D are used to identify potential structural factors governing carnallitite deformation and failure, whereas the creep tests on Groups A and B independently characterize seam-specific long-term deformation and load-bearing capacity. Accordingly, the linkage between the multiscale observations and creep behavior is interpreted as complementary mechanistic evidence rather than a direct specimen-to-specimen correlation. The specimens used for the short-term mechanical comparison were selected for the assigned experimental tasks and should therefore be regarded as task-specific laboratory specimens rather than as a random statistical sample of the entire deposit. Accordingly, the statistical results reported below are used primarily for descriptive comparison within the present specimen sets.

First, Group C carnallitite and Group D halite-dominated rock salt were subjected to short-term uniaxial compression with simultaneous AE monitoring, followed by SEM characterization at the Institute of Geology, Chinese Academy of Geological Sciences (Beijing, China). The specimens from Group C and D had diameters of approximately 50 mm and heights of 100 mm, resulting in height-to-diameter ratios close to 2:1. Uniaxial compression tests were conducted using a GAW-2000 electrohydraulic servo-controlled rigid testing machine (Chaoyang Test Instrument Co., Ltd., Changchun, China), which has a maximum axial capacity of 2000 kN. Each specimen was centered between the loading platens, and the spherical seat was adjusted to ensure uniform contact at both ends. The specimens were then subjected to continuous loading until failure under displacement control, during which axial load, deformation, peak strength, and macroscopic failure modes were recorded.

AE monitoring was conducted throughout the uniaxial compression tests using an Itasca AE system, which consists of a 12-channel Richter continuous-acquisition unit, pulse amplifiers, PAC Nano30 sensors (Physical Acoustics, MISTRAS Group, Princeton Junction, NJ, USA), and InSite-Lab data-processing software, version 3.16 (Itasca Consulting Ltd., Shrewsbury, UK). The sampling rate was set at 10 MS/s per channel. Following failure, representative fresh fracture surfaces were selected for SEM and energy-dispersive spectroscopy (EDS) analysis. Specimens from Groups C and D were examined using a JSM-5610LV scanning electron microscope (JEOL Ltd., Akishima, Tokyo, Japan). The crystal morphology, pore structures, microcracks, particle spalling, and interfaces between particles and the matrix were compared. Additionally, elemental composition was analyzed to assess compositional differences between carnallitite and halite-dominated rock salt.

Second, representative Group C carnallitite specimens were selected for CT scanning and three-dimensional reconstruction. A nanoVoxel-3502E X-ray microscope (Sanying Precision Instruments Co., Ltd., Tianjin, China), which boasts a nominal maximum spatial resolution of 500 nm, was employed to obtain internal tomographic images through helical scanning. The particle phase, matrix phase, and pore-fracture structure were identified and reconstructed in three dimensions. Additionally, particle volume, equivalent particle size, and spatial connectivity were quantified. These observations were compared with the uniaxial compressive strengths of the corresponding specimens to examine the relationships among particle scale, connectivity, particle–matrix distribution, and macroscopic load-bearing capacity. Based on the CT analysis, a PFC3D particle-flow model of carnallitite was established and calibrated against the uniaxial compression response of the representative Group C specimens. The numerical results were primarily utilized for particle-size-distribution sensitivity analysis and, in conjunction with CT and SEM observations, to interpret how the internal particle-contact network and weak interfaces influence macroscopic load-bearing capacity.

Finally, single-specimen multistage creep tests were conducted on Groups A and B carnallitite using an SLB100 triaxial rheological testing machine (Changchun Machinery, Changchun, China). The apparatus featured a maximum axial loading capacity of 100 kN, a force-measurement accuracy of ±1% of the indicated value, an axial deformation measurement range of 0–10 mm, and a deformation accuracy of ±0.003 mm. The creep specimens had diameters ranging from 48 to 54 mm and height-to-diameter ratios of 2.0 to 2.5. Errors in specimen height and diameter were limited to ±0.3 mm, end-face unevenness to ±0.05 mm, and end-face perpendicularity relative to the specimen axis to ±0.25°. The test temperature was maintained at 27 ± 1 °C, with relative humidity set between 45% and

60%. To minimize moisture absorption and deliquescence, petroleum jelly was uniformly applied to the surfaces of the specimens.

Due to the distinct origins of Groups A and B from different carnallitite seams, as well as their variations in short-term strength and long-term load-bearing capacity, the creep stress levels were selected independently for each group rather than applying a uniform absolute stress sequence. Group A was subjected to stress levels of 2.0, 3.0, 3.5, 4.0, and 5.0 MPa, while Group B experienced stress levels of 2.0, 3.0, 4.0, 5.0, and 5.5 MPa. These sequences were specifically designed to encompass low-stress stable creep, the critical transition phase, and high-stress accelerating creep for each group. Each stress level was achieved within approximately 1–2 min and subsequently maintained at a constant value. When the displacement increment decreased to below 0.001 mm/h, the creep at that stress level was considered essentially stabilized, prompting the application of the next stress level. If the strain rate continued to rise, the current stress was sustained until the specimen entered accelerating creep and ultimately failed. Axial and radial deformation histories were recorded to characterize the primary (decelerating), steady-state, and accelerating creep phases. The long-term strengths of both groups were estimated using the specific failure energy method, and the parameters of the Burgers model were inverted and assessed for goodness of fit. The resulting long-term strengths and creep parameters were then employed in the structural-parameter analysis of the stope.

The overall program thus comprised short-term uniaxial compression, AE monitoring, CT, SEM, PFC sensitivity analysis, and multistage creep testing. Unified specimen identifiers were utilized to establish correspondence among the various test batches, measurements, and subsequent analyses.

3. Compressive Failure Characteristics of Carnallitite Relative to Halite-Dominated Rock Salt

Using Group D halite-dominated rock salt as a reference, this section analyzes the strength, deformation, damage evolution, and microfailure characteristics of Group C carnallitite under short-term uniaxial compression. The results elucidate the short-term mechanical responses of both Groups C and D, thereby establishing a foundation for the subsequent analysis of microstructural controls in Group C.

3.1. Differences in Uniaxial Compression Response

The uniaxial compression results for Group D, which is characterized by halite-dominated rock salt, and Group C, represented by carnallitite, are presented in Table 2. The two specimen groups exhibit marked differences in both the observed strength levels and within-group dispersion. The average uniaxial compressive strength (UCS) of Group D rock salt is measured at 28.24 MPa, in contrast to the representative specimens of Group C carnallitite, which show an average UCS of only 7.83 MPa, representing merely 27.7% of Group D's average. Furthermore, the maximum-to-minimum strength ratio for Group D is approximately 1.23, whereas for Group C it is 2.58.

Considering the limited sample sizes, additional descriptive statistics were calculated to characterize the present specimen sets. For Group C (n = 5), the mean UCS was 7.83 MPa, with a standard deviation of 2.90 MPa, a coefficient of variation of 37.1%, a median of 7.46 MPa, an interquartile range of 6.28–7.96 MPa, and a 95% confidence interval with a mean of 4.22–11.43 MPa. For Group D (n = 4), the corresponding values were 28.24 MPa, 2.53 MPa, 9.0%, 28.42 MPa, 26.74–29.91 MPa, and 24.21–32.26 MPa, respectively. However, because of the small, task-specific specimen sets, these statistics should not be interpreted as population-level estimates or as evidence of universally significant differences between the two lithologies. Together with the coefficient of variation of 37.1% for Group C compared with 9.0% for Group D, these descriptive statistics indicate greater within-group dispersion in Group C within the present specimen sets.

Table 2. Uniaxial compression results for Group D halite-dominated rock salt and Group C carnallitite.

Specimen Group	Specimen ID	UCS/MPa	Mean/MPa
Group D halite-dominated rock salt	D-1	27.26	28.24
	D-2	29.58	
	D-3	25.19	
	D-4	30.91	
Group C carnallitite	C-1	12.56	7.83
	C-2	4.87	
	C-3	7.96	
	C-4	6.28	
	C-5	7.46	

Representative uniaxial stress–strain curves and failure modes for Groups D and C are presented in Figure 2. The rock-salt specimens from Group D demonstrated higher peak strengths, smoother pre-peak curves, and a more continuous load-bearing process, indicating a more uniform internal structure and stable stress-transfer paths. As summarized in Table 2, the average uniaxial compressive strength (UCS) of Group D was substantially higher than that of Group C, confirming the pronounced strength difference between the two lithologies. Although the failure modes included splitting, crushing, and end-cone failure, the strengths were relatively concentrated, suggesting that internal structural differences had a limited impact on macroscopic strength. In contrast, Group C carnallitite exhibited shear, splitting, crushing, and composite failure, accompanied by more variable post-peak responses. Consequently, its compressive failure was more significantly influenced by the particle–matrix structure and local weak interfaces. These differences may be attributed to pores and fractures, weakly bonded surfaces, and particle–matrix interfaces within the carnallitite; the detailed microstructural mechanisms will be examined in Section 4.

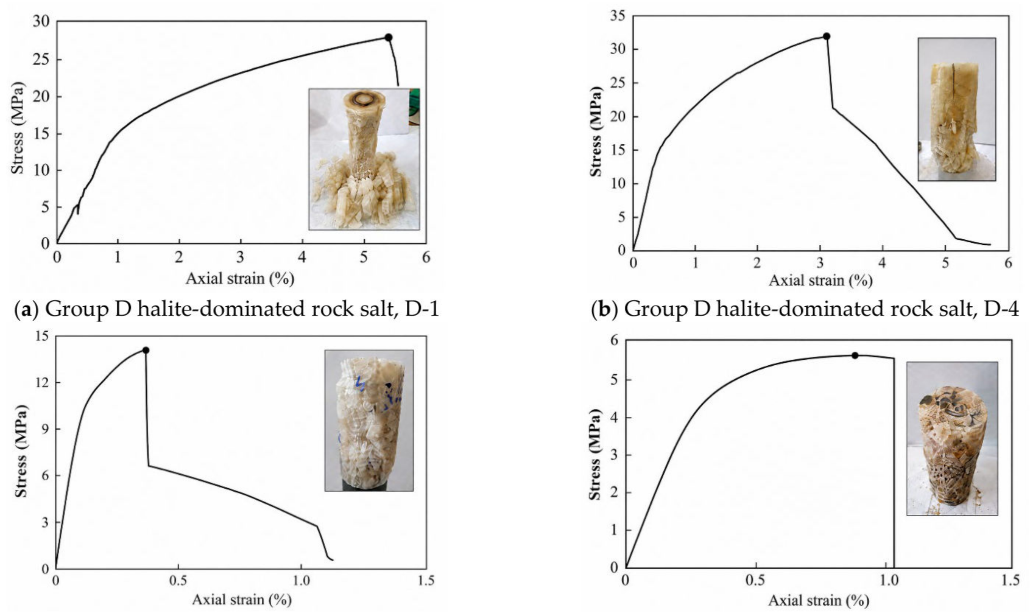

(**a**) Group D halite-dominated rock salt, D-1 (**b**) Group D halite-dominated rock salt, D-4

(**c**) Group C carnallitite, C-1 (**d**) Group C carnallitite, C-2

Figure 2. Comparison of uniaxial stress–strain curves and failure modes of Group D halite-dominated rock salt and Group C carnallitite.

3.2. Differences in AE-Based Damage Evolution

AE results provide further insight into the differences in internal crack activity during loading [26]. Representative examples were selected from Group D specimens D-2 and D-4, as well as Group C specimens C-1 and C-5, as illustrated in Figure 3. The rock-salt specimens from Group D exhibited a limited number of AE events during the initial loading stage, followed by a rapid increase in event count as the peak stress approached. Consequently, their damage evolution was characterized by weak early activity, concentrated pre-peak propagation, and a rapid release of energy upon failure.

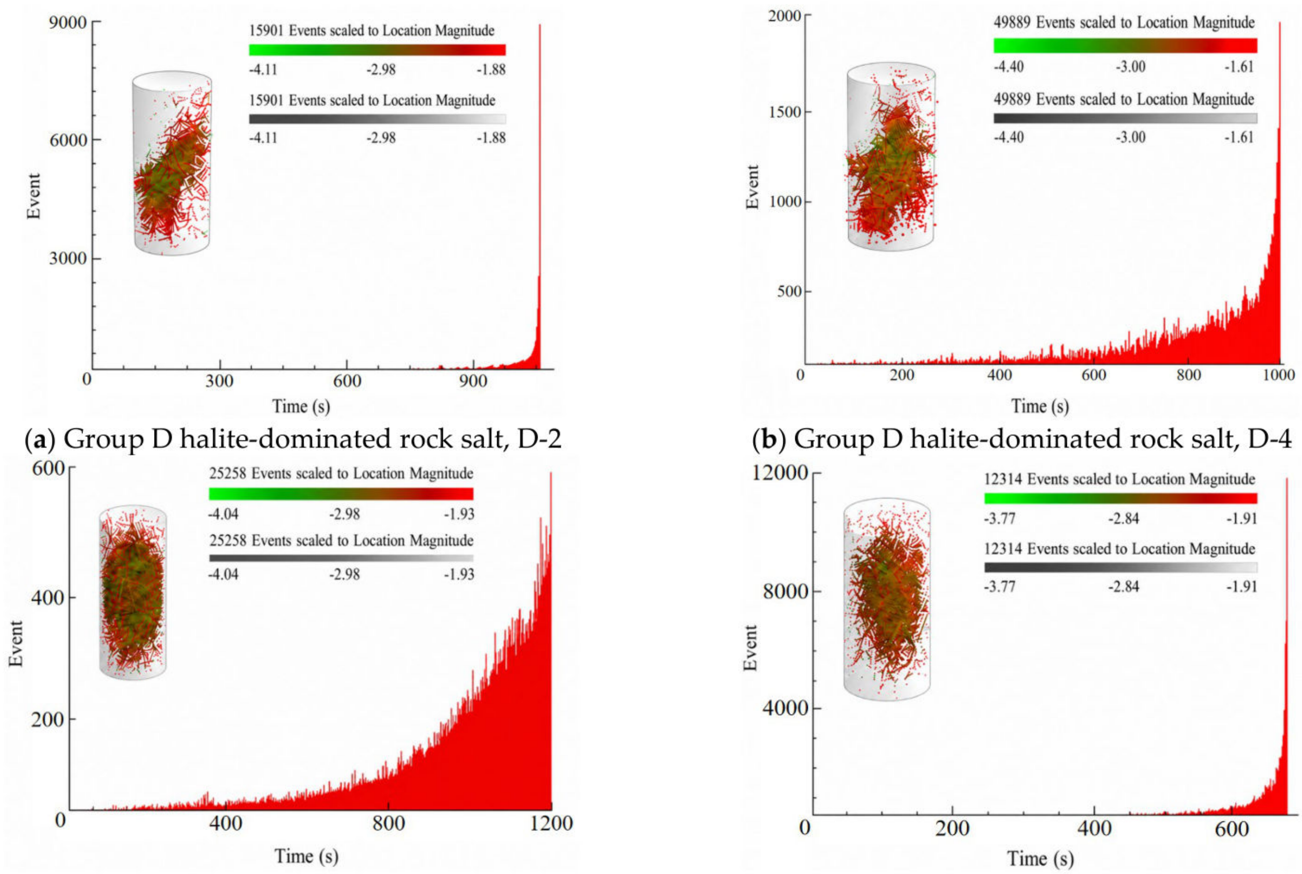

(**a**) Group D halite-dominated rock salt, D-2 (**b**) Group D halite-dominated rock salt, D-4

(**c**) Group C carnallitite, C-1 (**d**) Group C carnallitite, C-5

Figure 3. Comparison of AE responses during uniaxial compression of Group D halite-dominated rock salt and Group C carnallitite.

In comparison to Group D rock salt, the AE response of Group C carnallitite exhibited greater dispersion and intermittency. The AE activity in C-1 increased progressively during loading, indicating that multiple internal regions were involved in the damage evolution. In C-5, the event count surged rapidly during the pre-peak stage, reflecting a sudden destabilization of a local weak structure. Furthermore, AE source-location results revealed that events in Group C were distributed across several regions rather than being confined to a single macroscopic fracture plane. Consequently, factors such as particle-contact adjustment, particle–matrix separation, pore and crack closure, and sliding along weak interfaces likely contributed to the damage process.

The contrasting AE characteristics between Groups D and C confirm that their compressive damage evolves through distinct mechanisms. In Group D rock salt, damage was primarily characterized by relatively continuous crack propagation and concentrated pre-peak failure. Conversely, in Group C carnallitite, the complex particle–matrix structure and numerous weak interfaces rendered damage more sensitive to local structural features, resulting in multisource and spatially non-uniform evolution.

3.3. SEM Comparison of Microstructures

To elucidate the differences in macroscopic strength and AE response, representative fracture surfaces of the failed Group D rock salt and Group C carnallitite were examined using SEM, as illustrated in Figure 4. The fracture surfaces of Group D exhibited a relatively simple structure with distinctly defined crystal morphologies. The failure mechanisms were primarily characterized by crystal breakage, intergranular cracking, and localized crushing. The relatively continuous crystal contacts promoted stable stress-transfer pathways, which correlates with the higher and less variable UCS observed in Group D.

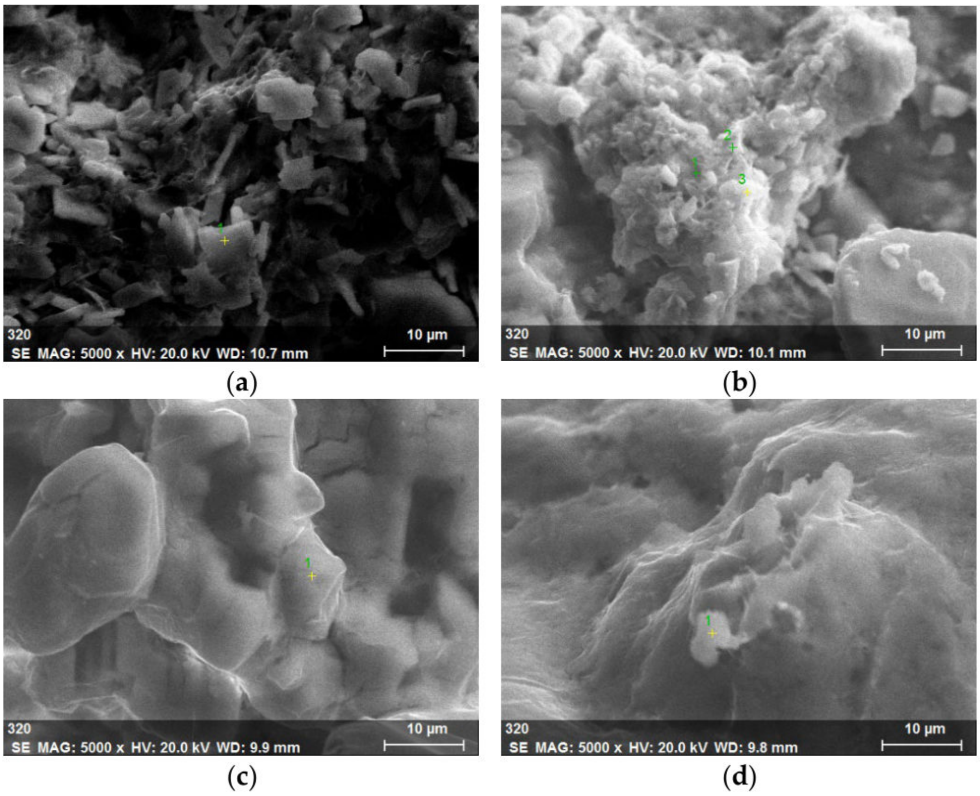

Figure 4. SEM comparison of the microstructures of Group D halite-dominated rock salt and Group C carnallitite. (**a**) Group D halite-dominated rock salt, D-2; (**b**) Group D halite-dominated rock salt, D-3; (**c**) Group C carnallitite, C-1; (**d**) Group C carnallitite, C-5.

The fracture surfaces of Group C carnallitite exhibited a distinctly more complex morphology, characterized by rough crystal faces, fragmented particles, pores, microcracks, and discontinuous contact interfaces. Certain regions contained relatively intact crystals with poor intercrystal connectivity, while other areas displayed particle spalling and localized fragmentation. Consequently, cracks preferentially propagated along particle boundaries, weakly bonded surfaces, or particle–matrix interfaces. Energy-Dispersive Spectroscopy (EDS) analysis revealed the presence of sodium (Na), calcium (Ca), and sulfur (S) alongside the major elements chlorine (Cl), potassium (K), and magnesium (Mg), suggesting greater compositional heterogeneity relative to Group D rock salt. The EDS results are used here only as qualitative evidence of compositional heterogeneity and are not intended as quantitative mineral-phase identification. Quantitative phase analysis, such as XRD/Rietveld characterization, was not performed in the present study.

The SEM comparison illustrates that the low strength and pronounced variability of Group C carnallitite cannot be solely attributed to the strength of individual mineral grains. Rather, these factors are closely linked to the particle–matrix structure, multiple mineral interfaces, and local pores and fractures. These microstructural weak zones facilitate local stress concentration during loading, leading to premature initiation and nonuniform propagation of microcracks. Therefore, the compressive failure of Group C carnallitite is strongly influenced by its microstructure. To quantify the effects of particle structure, connectivity, and crystal size on strength variability, the subsequent section integrates three-dimensional CT reconstruction with PFC simulation.

4. Microstructural Controls and Strength Characterization of Carnallitite

The comparison with Group D rock salt reveals that Group C carnallitite is characterized by low strength, significant variability, and complex failure modes. To elucidate these distinctive mechanical responses, this section integrates three-dimensional CT reconstruction, particle size statistics, and PFC simulation to analyze how the particle–matrix structure, particle size distribution, and weak interfaces influence the UCS.

4.1. Three-Dimensional CT Reconstruction and the Particle-Size-Strength Relationship

To investigate the microstructural origin of strength variability in Group C, specimens C-1 and C-2 were selected for comparative three-dimensional CT reconstruction. Specimen C-1, characterized by relatively high strength, and specimen C-2, identified as low strength, were chosen to examine the relationship between the particle–matrix structure and macroscopic strength. The reconstructions are illustrated in Figure 5. In specimen C-1, the particle phase exhibited relative continuity and formed a more complete spatial network, whereas the particles in specimen C-2 were more dispersed and less interconnected. This contrast suggests that the load-bearing capacity of Group C carnallitite is influenced not only by mineral composition but also by the formation of an effective load-bearing skeleton by the particles. When connectivity is high, external loads can be transmitted more continuously through the particle skeleton, thereby reducing local stress concentration. Conversely, when particles are dispersed, load transfer becomes increasingly reliant on particle–matrix interfaces, which are more susceptible to crack initiation and propagation. The contrasting CT characteristics of C-1 and C-2 suggest that particle connectivity may be associated with differences in macroscopic strength. However, because the detailed comparison involves only two representative specimens, this observation should be regarded as qualitative structural evidence. A larger CT-characterized specimen set would be required to establish and quantify the relationship between particle-network characteristics and UCS.

To quantify the influence of particle scale on the strength of Group C carnallitite, the average particle volume was calculated from the three-dimensional CT reconstructions and compared with UCS, as shown in Figure 6.

Average particle volume was generally negatively correlated with UCS and can be expressed as follows:

$$\sigma_c = -0.066V + 8.64R^2 = 0.94 \tag{1}$$

where σ_c is the uniaxial compressive strength in MPa and V is the converted average particle volume in mm^3.

For the five independent Group C specimens examined (n = 5), the UCS generally decreased as the average particle volume increased. Although the fitted relationship yielded $R^2 = 0.94$, the small sample size limits statistical inference. Equation (1) is therefore used only to describe the observed trend within the present dataset and should not be interpreted as a statistically validated predictive relationship or a universal scaling law for carnallitite. Larger particles may accentuate stiffness contrasts and local stress concentrations near

https://doi.org/10.3390/pr14162631

particle–matrix interfaces, whereas smaller and more uniformly distributed particles may provide more alternative stress-transfer paths. The strength of Group C carnallitite is nevertheless jointly influenced by particle connectivity, mineral assemblage, weak interfaces, and local pores or fractures.

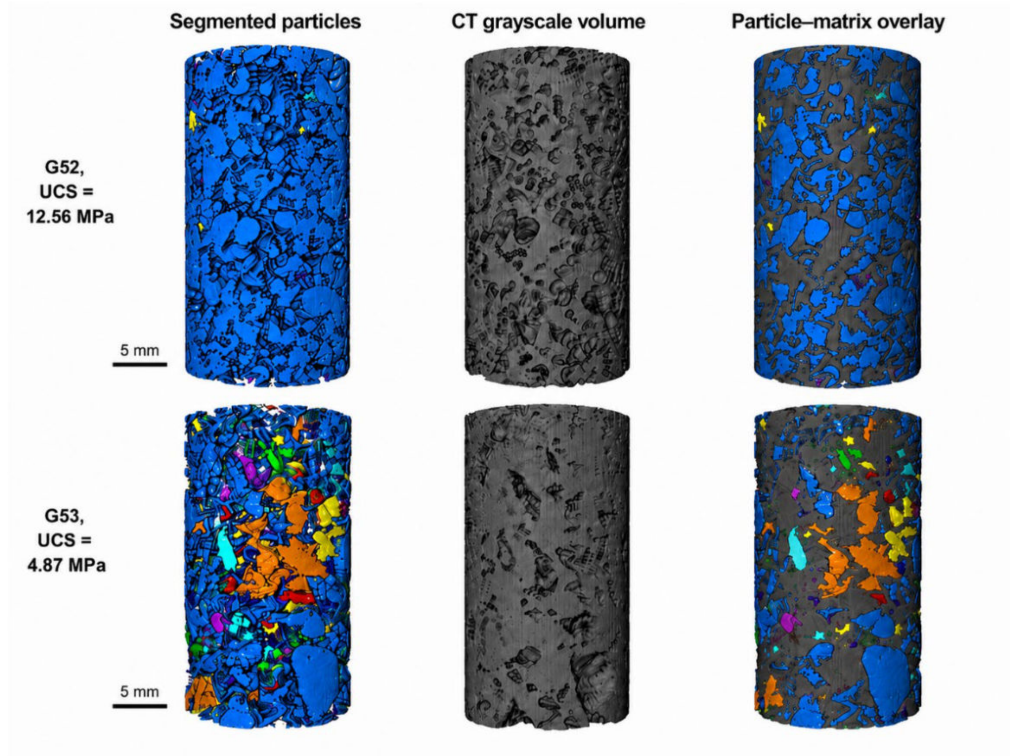

Figure 5. Three-dimensional CT reconstructions of representative Group C carnallitite specimens.

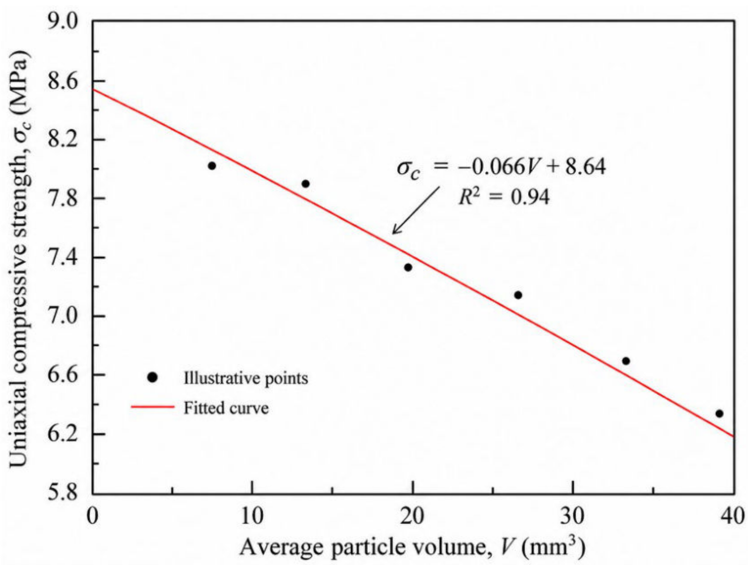

Figure 6. Relationship between average particle volume and UCS for Group C carnallitite.

4.2. Numerical Verification of Particle-Size-Distribution Effects

The three-dimensional CT reconstructions and average particle-volume statistics revealed an observed relationship between particle scale and the UCS of Group C carnallitite. Particle flow methods represent compressed-rock response through particle contacts and bond breakage and are therefore useful for sensitivity analyses of particle-scale characteristics [27]. To assess the influence of particle-size-distribution dispersion, PFC uniaxial compression simulations were conducted for several prescribed particle-size ranges. The model was calibrated against the uniaxial compression response of specimen C-3 from Group C.

A cylindrical PFC3D specimen with a diameter of 50 mm and a height of 100 mm was established using a linear parallel-bond contact model. The calibration target was specimen C-3, whose experimental UCS was 7.96 MPa. After microparameter calibration, the numerical specimen yielded a UCS of 7.82 MPa. The calibrated contact and bond parameters listed in Table 3 were subsequently kept unchanged in the particle-size-distribution sensitivity simulations.

Table 3. Calibrated microparameters used in the PFC3D model.

Parameter	Symbol	Value
Effective modulus	E	6.5 GPa
Normal-to-shear stiffness ratio	k	0.8
Friction coefficient	μ	0.45
Parallel-bond effective modulus	—	1.5 GPa
Parallel-bond stiffness ratio	—	1.2
Normal bond strength	—	67.2 MPa
Shear bond strength	—	56.0 MPa
Friction angle	φ	35°

In the first sensitivity series, a mean particle size of 4.0 mm was adopted as a controlled reference so that the effect of distribution span could be examined while the mean value remained fixed. Numerical specimens with size ranges of 0.4–8.0, 1.0–7.0, 2.0–6.0, 3.0–5.0, and 4.0–4.0 mm were then generated using the same calibrated microparameters. The corresponding results are summarized in Table 4.

Table 4. PFC-simulated UCS values for different particle-size distributions.

Minimum Particle Size/mm	Maximum Particle Size/mm	Mean Particle Size/mm	UCS/MPa
0.4	8.0	4.0	7.82
1.0	7.0	4.0	7.78
2.0	6.0	4.0	9.13
3.0	5.0	4.0	8.71
4.0	4.0	4.0	10.40

As demonstrated in Table 4, when the mean particle size is fixed at 4.0 mm, the simulated UCS generally increases as the prescribed particle-size range narrows, although fluctuations are observed among individual cases. Narrowing the range from 0.4–8.0 mm to 4.0–4.0 mm increases the simulated UCS from 7.82 to 10.40 MPa, an increase of approximately 33.0%. The response is not strictly monotonic: the strengths for the 1.0–7.0 mm and 3.0–5.0 mm cases are lower than those of adjacent cases. This indicates that the simulated strength is affected not only by the prescribed size range but also by random particle arrangement, local coordination, and contact-network variability. The present simulations use one realization for each prescribed particle-size distribution; therefore, they are interpreted as a sensitivity analysis rather than a statistical characterization of PFC variability. Repeated stochastic realizations are required to quantify this variability in future work.

A second archived numerical series provides supplementary evidence regarding changes in mean particle size. With the minimum particle size fixed at 0.4 mm, increasing the maximum particle size from 4.5 to 8.0 mm changed the corresponding mean particle size from 2.45 to 4.20 mm, while the simulated UCS values were 9.50, 8.66, 9.03, 6.93, and 7.82 MPa for maximum sizes of 4.5, 5.0, 6.0, 7.0, and 8.0 mm, respectively. Because these simulations were not designed as a full factorial gradation study, the effects of particle-size span, mean size, and gradation coefficient cannot be interpreted as completely independent factors.

In conjunction with the CT and SEM observations of Group C carnallitite, the simulations suggest that particle-size-distribution heterogeneity can influence macroscopic load-bearing capacity. A broader distribution may be associated with more spatially variable local contacts and greater reliance on particle–matrix interfaces in some regions, whereas a narrower distribution may favor more regular packing under the prescribed numerical conditions. However, quantitative contact-network descriptors such as coordination number, force-chain statistics, and fabric anisotropy were not extracted in the present simulations. Accordingly, changes in contact-network uniformity are treated here as a mechanistic interpretation rather than direct quantitative evidence. Overall, the PFC results indicate sensitivity of simulated macroscopic strength to the prescribed particle-size distribution and do not establish a deterministic particle-size-to-UCS law.

4.3. Particle–Matrix Weak-Interface Mechanism

The compression failures, CT reconstructions, average particle volume strength relationship, and PFC strength responses collectively indicate that the low strength and pronounced variability of Group C carnallitite are closely associated with weak interfaces between particles and the matrix, as well as structural heterogeneity. In contrast to the relatively continuous crystal contacts and concentrated crack paths observed in Group D rock salt, Group C displays significant particle size differences, insufficient particle connectivity, and well-developed interfaces between particles and the matrix, along with pores and fractures. These factors contribute to the formation of multiple microstructural weak zones.

As illustrated in Figure 7, the mechanism can be divided into three stages: compaction adjustment, crack initiation and propagation, and coalescence failure. In Figure 7a, the heterogeneous structure is composed of particles, matrix, pores, and weak interfaces. During the initial loading phase, adjustments in particle contacts, pore compression, and the closure of weakly bonded surfaces lead to significant initial nonlinearity. In Figure 7b, as stress increases, the disparities in stiffness and bond strength between particles and the matrix become more pronounced, resulting in local stress concentrations near particle boundaries, weakly bonded surfaces, and pores. Microcracks preferentially initiate at these vulnerable locations and progressively propagate. In Figure 7c, these cracks connect and coalesce along adjacent weak interfaces, forming a dominant fracture path that ultimately destabilizes the load-bearing structure, resulting in shear, splitting, crushing, or composite failure. Thus, the compressive failure of Group C carnallitite can be understood as a process in which structural heterogeneity induces local stress concentrations that subsequently govern crack evolution and macroscopic instability.

Compressive failure in Group C carnallitite does not stem from an overall instability governed by a single dominant crack; instead, it arises from accumulated damage across multiple weak zones, followed by the coalescence of a preferential fracture path. This mechanism elucidates both the variability in strength and the complexity of failure modes in Group C, offering a microstructural basis for understanding interface sliding and damage accumulation under prolonged loading.

https://doi.org/10.3390/pr14162631

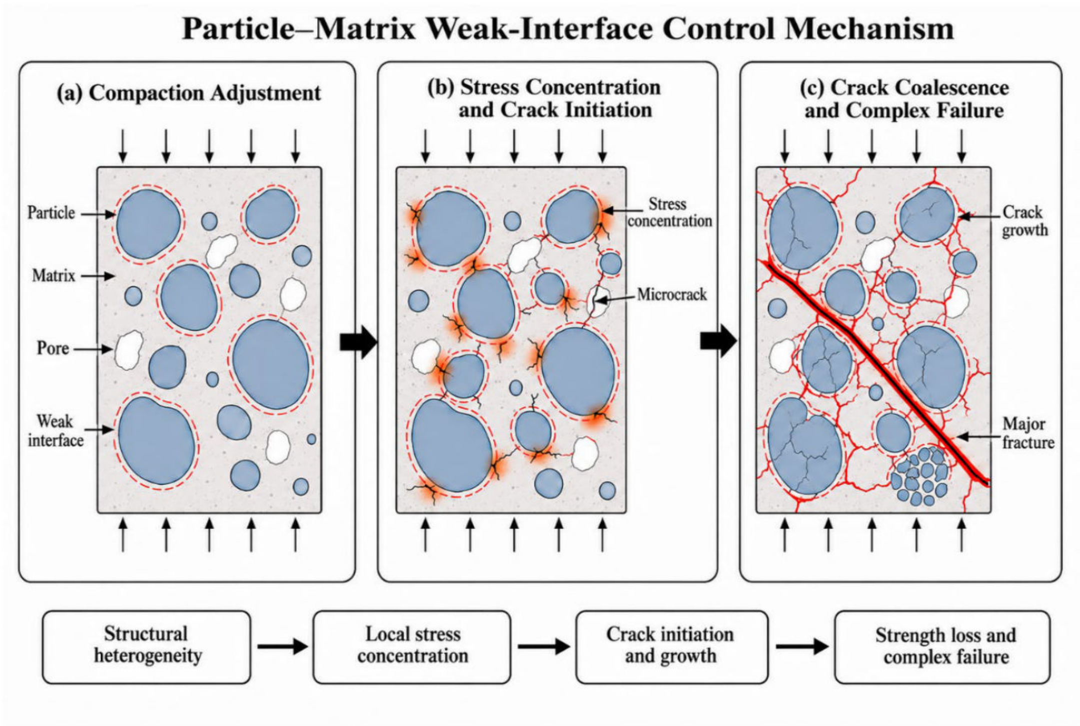

Figure 7. Schematic illustration of the particle–matrix weak-interface control mechanism in Group C carnallitite.

5. Long-Term Creep Behavior of Carnallitite and Implications for Stress-Relief Mining

The comparison between Groups C and D indicates that Group C carnallitite exhibits relatively low strength and significant structural variability. Its short-term compressive failure is closely linked to weak interfaces between particles and the matrix, as well as the presence of local pores and fractures. These structural characteristics may also affect particle-contact adjustments, interface sliding, and damage accumulation under prolonged loading conditions. Groups A and B, along with Group C, were derived from different experimental batches; therefore, the multiscale results presented in Sections 3 and 4 provide a structural context for the time-dependent deformation of carnallitite but cannot be regarded as direct evidence of microstructural differences between Groups A and B. Consequently, the stability assessment of carnallitite stopes must rely on the creep responses, long-term strengths, and seam-specific differences in Groups A and B.

Accordingly, no direct quantitative mapping between the microstructural characteristics of Group C and the creep parameters of Groups A and B is attempted in this study.

5.1. Creep Response and Long-Term Strength

The creep strain-time curves for Groups A and B carnallitite at varying stress levels are illustrated in Figure 8. At lower stress levels, the creep strain exhibited a gradual increase and the curves stabilized, primarily demonstrating primary (decelerating) and steady-state creep behavior. As the stress increased, the creep strain significantly increased, and the strain rate accelerated during the late stages of several high-stress curves. Group A displayed pronounced deformation growth at stress levels of 3.5 MPa and above, while Group B exhibited a clear accelerating trend, particularly at 5.0 and 5.5 MPa. These observations indicate that Group B exhibited relatively higher resistance to creep deformation under comparable stress conditions, which is consistent with the subsequent long-term strength estimates.

The multistage creep curves also provide an experimental bracket for the transition in long-term load-bearing behavior. For Group A, stable creep was observed up to 3.0 MPa, whereas pronounced accelerating deformation appeared from approximately 3.5 MPa, giving a transition interval of 3.0–3.5 MPa. For Group B, the corresponding transition occurred between 4.0 and 5.0 MPa, with clear accelerating behavior at the higher stress levels.

Specimen morphologies before and after creep testing are illustrated in Figure 9. Both Groups A and B exhibited axial deformation alongside varying degrees of local fragmentation following prolonged loading, indicating that sustained creep can lead to observable local damage. As the internal structure was not imaged in situ during the creep process, the detailed evolution of internal cracks and interfacial damage necessitates verification through future microstructural observations.

The observed creep responses align phenomenologically with the particle–matrix weak-interface mechanism proposed in Section 4. The results from short-term compression, SEM, and CT suggest that particle-contact adjustments, weak-interface sliding, and local damage accumulation may collectively contribute to creep deformation under sustained loading. This interpretation represents a mechanistic inference drawn from multiple experimental observations, rather than a direct observation of interface evolution during creep.

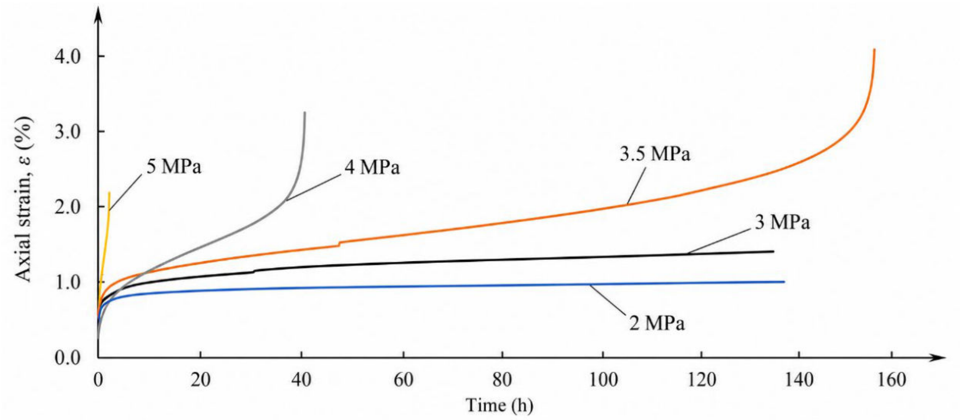

(**a**) Group A carnallitite

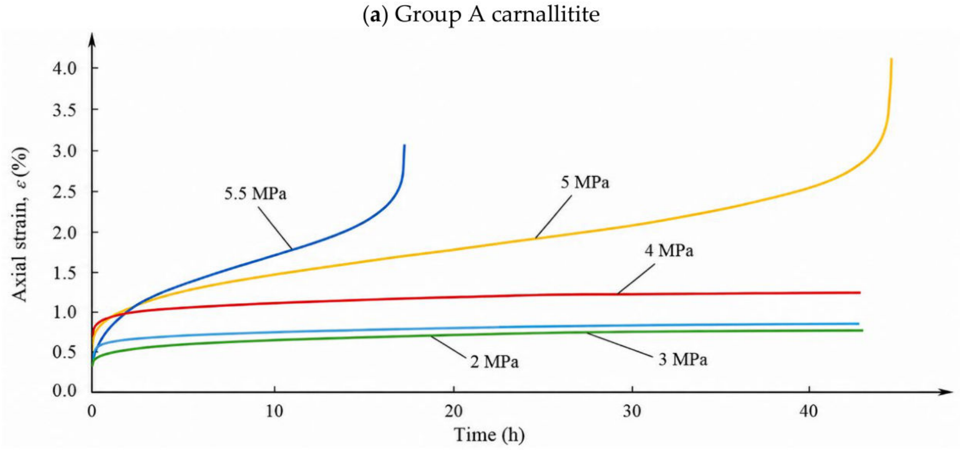

(**b**) Group B carnallitite

Figure 8. Creep strain-time curves of Group A and B carnallitite at different stress levels.

To evaluate long-term load-bearing capacity, the specific-failure-energy analysis [28] was used to refine the experimentally bracketed transition intervals, as illustrated in Figure 10. For each loading level, the energy response associated with deformation was evaluated, and a pronounced energy-surge region was identified as the creep response changed from stable deformation to unstable failure. The intersection defined by the adjacent points around the creep-failure energy-surge zone and the upper boundary of the uniaxial failure-energy domain was used to estimate the long-term-strength threshold This procedure yielded approximately 3.3 MPa for Group A and 4.8 MPa for Group B, both of which fall within the transition ranges indicated by the creep curves. These values are therefore interpreted as method-specific long-term-strength estimates rather than uniquely validated material constants. Independent cross-validation using alternative criteria, such as isochronous stress-strain analysis or steady-state creep-rate thresholds, was not performed in the present study and is required for further verification.

(**a**) Group A carnallitite (**b**) Group B carnallitite

Figure 9. Group A and B carnallitite specimens before and after creep testing.

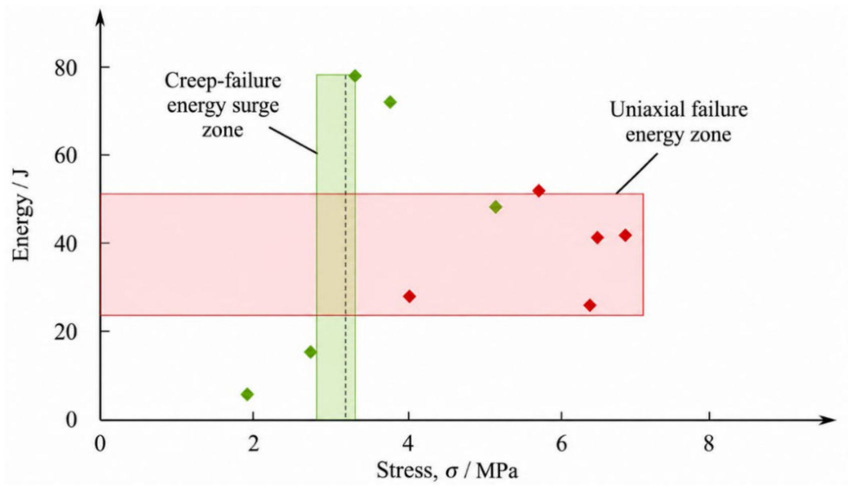

(**a**) Stress–energy relationship for Group A carnallitite

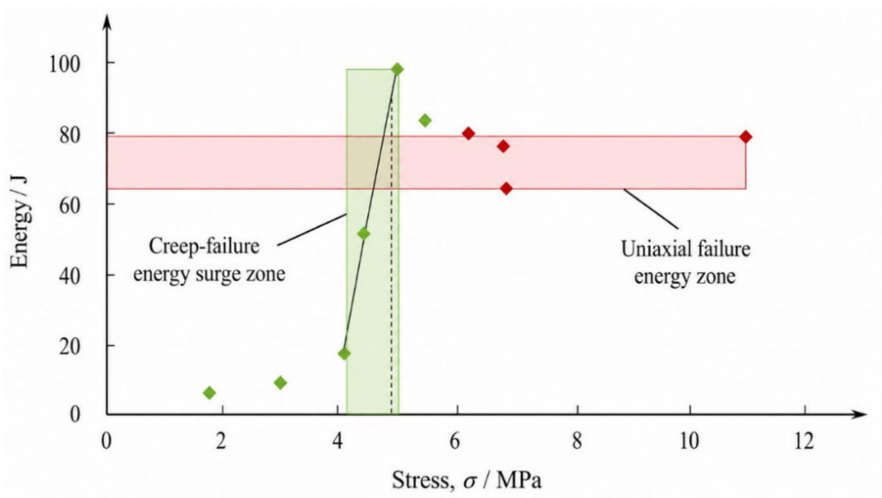

(**b**) Stress–energy relationship for Group B carnallitite

Figure 10. Long-term strength estimates for Group A and B carnallitite based on specific failure energy.

5.2. Fitting and Parameter Analysis of the Modified Burgers Model

To quantitatively describe the time-dependent deformation of Groups A and B, a modified Burgers model was fitted to the creep strain-time data across various stress levels. The classical Burgers model accounts for instantaneous elastic deformation, primary creep [29,30] and steady-state creep but cannot, by itself, represent post-yield irreversible deformation. The use of a Mohr–Coulomb plastic element in rheological models is established in rock-mechanics literature; therefore, the present modification is not proposed as a new constitutive topology. It is adopted here because the carnallitite creep curves show irreversible and accelerating deformation at elevated stress levels that cannot be represented solely by the viscoelastic components of the classical Burgers model. The configuration of the model is illustrated in Figure 11.

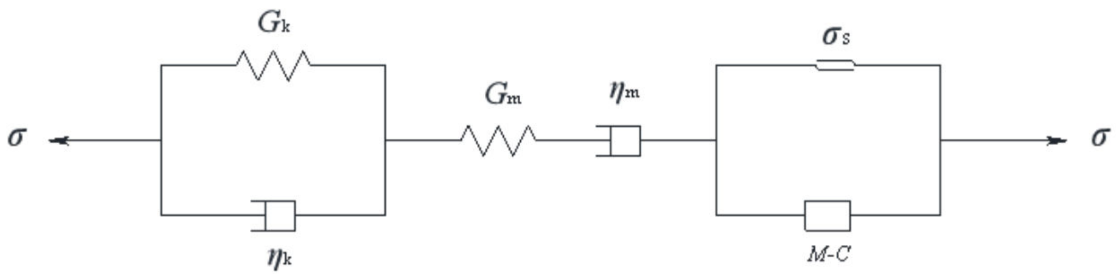

Figure 11. Modified Burgers model.

Before activation of the Mohr–Coulomb plastic element, the creep strain under constant axial stress is expressed as:

$$\varepsilon(t) = \frac{2\sigma}{9K} + \frac{\sigma}{3G_m} + \frac{\sigma}{3\eta_m}t + \frac{\sigma}{3G_k}\left[1 - \exp\left(-\frac{G_k}{\eta_k}t\right)\right] \tag{2}$$

where ε is the axial strain at time t; σ is the constant axial stress; K is the bulk modulus; G_m and ηm are the elastic modulus and viscosity coefficient, respectively, of the Maxwell element; and G_k and η_k are the elastic modulus and viscosity coefficient, respectively, of the Kelvin element. When the stress state reaches the Mohr–Coulomb yield condition, the plastic element becomes active. Under the present uniaxial creep condition, σ_3 = 0. The viscoelastic parameters G_m, G_k, η_m, and η_k are identified from the creep curves as described below, while the Mohr–Coulomb element represents the onset and subsequent irreversible plastic deformation rather than an independently validated new predictive plasticity model.

Model parameters were identified separately for Groups A and B at each stress level. The parameter identification process was based on the strain characteristics observed during the initial loading, primary creep, and steady-state creep stages. Specifically, the slope of the steady-state segment was primarily utilized to determine the viscosity coefficient of the Maxwell element, while the initial strain was employed to ascertain the elastic modulus of the Maxwell element. Additionally, the primary creep segment was used to identify both the elastic modulus and viscosity coefficient of the Kelvin element. The parameters identified at each individual stress level were statistically processed to derive representative within-group values, as presented in Table 5.

For each stress level, the axial stress, test duration, and identified parameters were substituted into the modified Burgers constitutive equation to compute strain at the experimental sampling times. Subsequently, the experimental and calculated axial strains were compared point by point at the same stress level and sampling time. All valid data from the stress levels of each group were pooled, and the coefficient of determination (R^2) and root-mean-square error ($RMSE$) were employed to assess the overall fitting quality.

$$R^2 = 1 - \frac{\sum_{i=1}^{n} \left(\varepsilon_{\exp,i} - \varepsilon_{\mathrm{fit},i}\right)^2}{\sum_{i=1}^{n} \left(\varepsilon_{\exp,i} - \bar{\varepsilon}_{\exp}\right)^2} \tag{3}$$

$$RMSE = \sqrt{\frac{1}{n}\sum_{i=1}^{n} \left(\varepsilon_{\exp,i} - \varepsilon_{\mathrm{fit},i}\right)^2} \tag{4}$$

where $\varepsilon_{\exp,i}$ and $\varepsilon_{\mathrm{fit},i}$ are the experimental and model-calculated axial strains, respectively, at sampling time i; $\bar{\varepsilon}_{\exp}$ is the mean experimental axial strain; and n is the number of valid data points used in the fitting assessment. Axial strain is expressed as a percentage; therefore, $RMSE$ represents the deviation between the experimental and calculated values in percentage points of strain.

Table 5. Modified Burgers model parameters and fitting metrics for carnallitite.

Specimen Group	G_m/GPa	G_k/GPa	η_m/(GPa·h)	η_k/(GPa·h)	R^2	$RMSE$/%
Group A carnallitite	0.20	0.31	11.64	0.92	0.957	0.0803
Group B carnallitite	0.23	0.48	13.93	0.87	0.964	0.0552

Note: Model parameters are representative within-group values obtained by statistical processing of the parameters identified at each stress level. R^2 and $RMSE$ were calculated by pooling all valid experimental and model-calculated strains within each group after separate parameter identification and model back-calculation at each stress level. Because axial strain is expressed as a percentage, $RMSE$ represents the deviation in percentage points of strain.

As shown in Table 5, the R^2 values for Groups A and B were 0.957 and 0.964, respectively, while the corresponding $RMSE$ values were 0.0803 and 0.0552 percentage points of strain. The modified Burgers model, therefore, accurately reproduced the overall creep-strain evolution of both groups within the stress levels and observation durations considered.

Compared to Group A, Group B exhibited a slightly higher R^2 and a lower $RMSE$, indicating a smaller overall discrepancy between the measured and calculated strains. The fitting quality was sufficient for comparing creep parameters and deformation characteristics in this study. It is important to emphasize that R^2 and $RMSE$ quantify the goodness of fit to the data used for parameter identification and do not represent predictive accuracy evaluated against an independent dataset.

The parameters in Table 5 indicate that G_m, G_k, and η_m were all higher for Group B, while η_k was similar for both groups. The higher elastic moduli and Maxwell viscosity coefficient suggest that Group B exhibited greater resistance to instantaneous elastic deformation, delayed elastic deformation, and steady-state creep, consistent with its higher long-term strength. These parameters are phenomenological quantities inverted from macroscopic creep curves and cannot independently establish specific differences in mineral composition, particle connectivity, or weak-interface development between the two groups.

Overall, under the present test conditions, the modified Burgers model adequately represented the creep-strain evolution of Groups A and B. The identified parameters and fitting metrics can be used to compare their overall rheological responses, but should not be directly extrapolated to different environmental conditions, complex stress paths, or long-term deformation that extends beyond the present observation period.

https://doi.org/10.3390/pr14162631

5.3. Implications for Stress-Relief Mining Design Constrained by Long-Term Strength

The study investigates two carnallitite seams within a potash mine, where stope stability is influenced by low strength, time-dependent deformation, and potential structural heterogeneity. The long-term strengths presented in Section 5.1 inform the design of stope support structures, while the model parameters discussed in Section 5.2 are primarily utilized to compare creep-deformation characteristics. These quantities serve distinct purposes and should not be used interchangeably. Consequently, stope structural parameters should not be determined solely based on short-term UCS; rather, long-term strength should serve as the primary mechanical constraint, augmented by creep parameters that account for deformation rate and delayed deformation.

The engineering calculation in this section is intended as a site-specific illustration rather than a universal pillar-design criterion. The investigated deposit is nearly horizontal and occurs at a mining depth of approximately 450 m. The representative stress-relief mining calculation combines collapse-arch-based span analysis with a long-term-strength-constrained inter-room pillar design. The adopted mining height is 6 m and the protected room span is 9 m (half span b_1 = 4.5 m). The unit weight is 0.021 MN/m^3, the effective overlying broken-rock thicknesses are 50 m for Group A and 53 m for Group B, and the pillar safety factor is n = 1.5. The long-term strengths used as mechanical constraints are 3.3 MPa and 4.8 MPa, respectively. The principal calculation inputs are summarized in Table 6.

Table 6. Principal input parameters for the representative inter-room pillar calculation.

Parameter	Group A	Group B
Mining depth	450 m	450 m
Mining height	6 m	6 m
Protected room span	9 m	9 m
Half span, b_1	4.5 m	4.5 m
Unit weight, γ	0.021 MN/m^3	0.021 MN/m^3
Effective overlying broken-rock thickness, h	50 m	53 m
Pillar safety factor, n	1.5	1.5
Long-term strength	3.3 MPa	4.8 MPa
Calculated inter-room pillar width	6 m	4 m

Using these site-specific inputs, the calculated inter-room pillar widths are approximately 6 m for Group A and 4 m for Group B. The simplified calculation adopts a quasi-static vertical-load representation based on the stress-relief/collapse-arch design framework and does not explicitly resolve the full three-dimensional in-situ stress field or lateral-stress coefficient. Accordingly, the calculated widths and extraction ratios are site-specific outputs under the stated assumptions and should not be generalized to other mines without project-specific geological, stress, geometric, and numerical verification.

Table 7 illustrates that, under the specified design conditions, the lower long-term strength of Group A is associated with both an inter-room pillar width and a stability-pillar width of 6 m. In contrast, the higher long-term strength of Group B is linked to widths of 4 m, with the panel extraction ratio increasing from 54% to 60%. This comparison indicates that, when other design conditions remain constant, the adopted long-term strength influences the dimensions of support structures and the calculated extraction ratio. For seams exhibiting lower long-term strength and more significant creep deformation, it is essential to prioritize the assessment of long-term support stability. Conversely, for seams with greater strength, a higher extraction ratio may be considered only after addressing the requirements related to roof and floor conditions, mining depth, disturbance range, and safety factors.

Table 7. Representative stope parameters constrained by the long-term strength of carnallitite.

Specimen Group	Long-Term Strength/MPa	Inter-Room Pillar Width/m	Stability-Pillar Width/m	Panel Extraction Ratio/%
Group A carnallitite	3.3	6	6	54
Group B carnallitite	4.8	4	4	60

Note: The parameters were compiled from the stress-relief mining design theory and the representative stope layout under the input conditions listed in Table 6. Long-term strength was obtained from laboratory creep tests and specific-failure-energy estimates. Actual engineering design must additionally account for seam occurrence, mining depth, roof and floor conditions, three-dimensional in-situ stress, stope layout, disturbance range, and the required safety factor.

Consequently, carnallitite stope parameters should not be determined using a single empirical value; instead, they should be zoned or classified based on seam-specific long-term strength, creep response, and structural heterogeneity. The analytical approach proposed here aims to identify potential weak structures through multiscale testing, characterize time-dependent deformation via creep tests and constitutive parameters, and subsequently refine stope-parameter calculations utilizing long-term strength. This methodology offers a reference for assessing the stability of deep carnallitite stopes, although the final parameters must be validated against site geology, in situ stress, and stope-scale numerical analyses.

6. Conclusions

This study investigated two carnallitite seams within a potash mine. Group C carnallitite and Group D halite-dominated rock salt were utilized for short-term compression tests and multiscale comparisons. In contrast, Groups A and B were employed for laboratory creep testing, long-term strength evaluation, and parameter analysis using a modified Burgers model. Additionally, PFC simulations were conducted to examine the effects of particle size distribution. The heterogeneous damage mechanisms responsible for the low strength of carnallitite, its long-term creep behavior, and the implications for stress-relief mining design were thoroughly evaluated. The main conclusions are as follows:

(1) The comparison between Groups C and D revealed that the representative carnallitite specimens from Group C exhibited markedly lower UCS and greater within-group dispersion than the Group D halite-dominated rock-salt specimens within the present dataset. The average UCS values of Groups D and C were 28.24 MPa and 7.83 MPa, respectively. The coefficients of variation were 9.0% for Group D and 37.1% for Group C, indicating greater dispersion in the Group C measurements. However, because the comparison is based on limited, task-specific specimen sets, these descriptive statistics should not be generalized as population-level statistical characteristics of the two lithologies. Additionally, the stress–strain curves and failure modes demonstrated that Group C exhibited a more pronounced initial compaction phase, sharper post-peak drops, and a wider variety of failure modes, reflecting its greater sensitivity to internal structural differences.

(2) The results from AE, SEM, and CT collectively elucidate the microstructural basis for the low strength observed in Group C carnallitite. The AE events were identified as multisource and locally intermittent, suggesting that the evolution of damage was not controlled by a single dominant crack. SEM analysis revealed rough crystal faces, localized pores, fragmented particles, multiple mineral interfaces, and weakly bonded structures. Furthermore, three-dimensional CT reconstruction demonstrated that the well-connected particle network in sample C-1 was associated with higher strength, while the more dispersed particles in sample C-2 were linked to lower strength. These observations suggest that particle connectivity and weak particle–matrix interfaces are potentially important structural factors affecting the load-bearing capacity of Group C carnallitite.

https://doi.org/10.3390/pr14162631

(3) Average particle-volume statistics and PFC simulations indicate that particle-scale characteristics are associated with Group C strength. For the five specimens examined, average particle volume showed a generally negative empirical relationship with UCS, but the limited sample size precludes interpretation as a universal predictive law. With a constant mean particle size of 4.0 mm in the first PFC sensitivity series, narrowing the prescribed size range from 0.4–8.0 mm to 4.0–4.0 mm increased simulated UCS from 7.82 to 10.40 MPa. Because one realization was used for each prescribed distribution and quantitative contact-network descriptors were not extracted, these simulations demonstrate sensitivity of macroscopic strength to the prescribed particle-size distribution rather than statistical validation of a unique contact-network mechanism.

(4) Groups A and B both exhibited pronounced time-dependent deformation, with method-specific long-term uniaxial strength estimates of approximately 3.3 MPa and 4.8 MPa, respectively. Within the current dataset, the modified Burgers model yielded R^2 values of 0.957 and 0.964 and *RMSE* values of 0.0803 and 0.0552 percentage points, respectively; these metrics quantify goodness of fit to the data used for parameter identification and do not constitute independent predictive validation. Under the site-specific design assumptions summarized in this study, the calculated inter-room pillar widths for Groups A and B were 6 m and 4 m, with corresponding panel extraction ratios of 54% and 60%. These engineering outputs should be recalculated when mining depth, stress state, geometry, roof/floor conditions, or safety requirements differ from those adopted here.

Future work should establish parallel specimen sets that directly couple creep testing of Groups A and B with CT/SEM characterization, and should use interrupted or in-situ observations to track creep-induced microcrack and interface evolution. Statistical robustness should be improved through larger sample sets and repeated PFC realizations with quantitative contact-network descriptors such as coordination number, force-chain statistics, and fabric anisotropy. The stress-relief mining design should be verified using three-dimensional stope-scale models incorporating field stress and geometry, together with systematic sensitivity analyses of mining depth, long-term strength, and safety factor. Coupled temperature-humidity-dissolution effects and time-dependent damage should also be incorporated into subsequent constitutive studies, and independent criteria should be used to cross-validate the long-term-strength estimates.

Author Contributions: Conceptualization, X.Q.; Methodology, H.W. (He Wang) and X.Q.; Software, H.W. (He Wang); Formal analysis, H.W. (He Wang) and L.C.; Investigation, H.W. (He Wang) and H.W. (Hui Wang); Resources, Z.W.; Validation, L.C.; Visualization, H.W. (Hui Wang); Supervision, X.Q. and Z.W.; Project administration, Z.W.; Writing—original draft, H.W. (He Wang); Writing—review and editing, X.Q. and L.C. All authors have read and agreed to the published version of the manuscript.

Funding: This research was funded by the National Natural Science Foundation of China (No. 52504086) and the Young Elite Scientist Sponsorship Program by the China Association for Science and Technology (CAST) (No. YESS20240093) and the Beijing Nova Program (No. 20230484242).

Data Availability Statement: The data presented in this study are available from the corresponding author upon reasonable request.

Conflicts of Interest: All authors were employed by the BGRIMM Technology Group. The authors declare that the research was conducted in the absence of any commercial or financial relationships that could be construed as a potential conflict of interest.

References

1. Mansouri, H.; Ajalloeian, R. Mechanical behavior of salt rock under uniaxial compression and creep tests. *Int. J. Rock. Mech. Min. Sci.* **2018**, *110*, 19–27. [CrossRef]

2. Bérest, P.; Gharbi, H.; Brouard, B.; Brückner, D.; DeVries, K.; Hévin, G.; Hofer, G.; Spiers, C.; Urai, J. Very slow creep tests on salt samples. *Rock. Mech. Rock. Eng.* **2019**, *52*, 2917–2934. [CrossRef]
3. Gharbi, H.; Bérest, P.; Blanco-Martín, L.; Brouard, B. Determining upper and lower bounds for steady state strain rate during a creep test on a salt sample. *Int. J. Rock. Mech. Min. Sci.* **2020**, *134*, 104452. [CrossRef]
4. Wang, J.; Zhang, Q.; Song, Z.; Zhang, Y. Creep properties and damage constitutive model of salt rock under uniaxial compression. *Int. J. Damage Mech.* **2020**, *29*, 902–922. [CrossRef]
5. Azabou, M.; Rouabhi, A.; Blanco-Martín, L.; Hadj-Hassen, F.; Karimi-Jafari, M.; Hévin, G. Rock salt behavior: From laboratory experiments to pertinent long-term predictions. *Int. J. Rock. Mech. Min. Sci.* **2021**, *142*, 104588. [CrossRef]
6. Ma, L.; Wang, Y.; Wang, M.; Xue, B.; Duan, L. Mechanical properties of rock salt under combined creep and fatigue. *Int. J. Rock. Mech. Min. Sci.* **2021**, *141*, 104654. [CrossRef]
7. Han, Y.; Ma, H.; Yang, C.; Li, H.; Yang, J. The mechanical behavior of rock salt under different confining pressure unloading rates during compressed air energy storage (CAES). *J. Pet. Sci. Eng.* **2021**, *196*, 107676. [CrossRef]
8. Zhao, K.; Ma, H.; Liang, X.; Li, X.; Liu, Y.; Cai, R.; Ye, L.; Yang, C. Damage evaluation of rock salt under multilevel cyclic loading with constant stress intervals using AE monitoring and CT scanning. *J. Pet. Sci. Eng.* **2022**, *208*, 109517. [CrossRef]
9. Li, Z.; Suo, J.; Fan, J.; Fourmeau, M.; Jiang, D.; Nelias, D. Damage evolution of rock salt under multilevel amplitude creep–fatigue loading with acoustic emission monitoring. *Int. J. Rock. Mech. Min. Sci.* **2023**, *164*, 105346. [CrossRef]
10. Blanco-Martín, L.; Azabou, M.; Rouabhi, A.; Hadj-Hassen, F. Laboratory experiments on rock salt and phenomenological observations. *Int. J. Rock. Mech. Min. Sci.* **2023**, *170*, 105452. [CrossRef]
11. Truster, T.J.; Moslehy, A.; Alshibli, K.A. Effects of crystal orientation, temperature, deviatoric stress, and confining stress on creep of rock salt. *Int. J. Rock. Mech. Min. Sci.* **2024**, *183*, 105913. [CrossRef]
12. Muhammad, N.; de Bresser, J.H.P.; Peach, C.J.; Spiers, C.J. Creep behaviour of bischofite, carnallite and mixed bischofite-carnallite-halite salt rock at in situ conditions. In *The Mechanical Behavior of Salt X*; CRC Press: London, UK, 2022; pp. 212–223. [CrossRef]
13. Cyran, K. The influence of impurities and fabrics on mechanical properties of rock salt for underground storage in salt caverns—A review. *Arch. Min. Sci.* **2021**, *66*, 155–179. [CrossRef]
14. Martin-Clave, C.; Ougier-Simonin, A.; Vandeginste, V. Impact of second phase content on rock salt rheological behavior under cyclic mechanical conditions. *Rock. Mech. Rock. Eng.* **2021**, *54*, 5245–5267. [CrossRef]
15. Liang, K.; Xie, L.Z.; He, B.; Zhao, P.; Zhang, Y.; Hu, W. Effects of grain size distributions on the macro-mechanical behavior of rock salt using micro-based multiscale methods. *Int. J. Rock. Mech. Min. Sci.* **2021**, *138*, 104592. [CrossRef]
16. Vandeginste, V.; Ji, Y.; Buysschaert, F.; Anoyatis, G. Mineralogy, microstructures and geomechanics of rock salt for underground gas storage. *Deep. Undergr. Sci. Eng.* **2023**, *2*, 129–147. [CrossRef]
17. Cyran, K.; Toboła, T.; Kamiński, P. Microfabrics impact on rock salt geomechanical diversity—An experimental investigation. *Eng. Geol.* **2024**, *336*, 107566. [CrossRef]
18. Kolano, M.; Cała, M.; Stopkowicz, A. Mechanical properties of rock salt from the Kłodawa Salt Dome—A statistical analysis of geomechanical data. *Materials* **2024**, *17*, 3564. [CrossRef] [PubMed]
19. Chen, J.; Peng, H.; Fan, J.; Zhang, X.; Liu, W.; Jiang, D. Microscopic investigations on the healing and softening of damaged salt by uniaxial deformation from CT, SEM and NMR: Effect of fluids (brine and oil). *RSC Adv.* **2020**, *10*, 2877–2886. [CrossRef] [PubMed]
20. Peng, H.; Fan, J.; Zhang, X.; Chen, J.; Li, Z.; Jiang, D.; Liu, W. Computed tomography analysis on cyclic fatigue and damage properties of rock salt under gas pressure. *Int. J. Fatigue* **2020**, *134*, 105523. [CrossRef]
21. Li, J.; Tang, Y.; Shi, X.; Xu, W.; Yang, C. Modeling the construction of energy storage salt caverns in bedded salt. *Appl. Energy* **2019**, *255*, 113866. [CrossRef]
22. Liu, W.; Zhang, Z.; Fan, J.; Jiang, D.; Daemen, J.J.K. Research on the stability and treatments of natural gas storage caverns with different shapes in bedded salt rocks. *IEEE Access* **2020**, *8*, 18995–19007. [CrossRef]
23. Song, H.; Zhu, S.; Li, J.; Wang, Z.; Li, Q.; Ning, Z. Design criteria for the construction of energy storage salt cavern considering economic benefits and resource utilization. *Sustainability* **2023**, *15*, 6870. [CrossRef]
24. Jenabidehkordi, A. Computational methods for fracture in rock: A review and recent advances. *Front. Struct. Civ. Eng.* **2019**, *13*, 273–287. [CrossRef]
25. Castro-Filgueira, U.; Alejano, L.R.; Mas Ivars, D. Particle flow code simulation of intact and fissured granitic rock samples. *J. Rock. Mech. Geotech. Eng.* **2020**, *12*, 960–974. [CrossRef]
26. Liu, J.F.; Wang, C.P.; Wang, L.; Ran, L.N.; Deng, C.F. Tensile failure and acoustic emission characteristics of rock salt under different tensile testing conditions. *J. Cent. South Univ.* **2023**, *30*, 1345–1358. [CrossRef]
27. Yiouta-Mitra, P.; Svourakis, K.; Nomikos, P. Particle flow numerical study of size effect on uniaxial compressive strength of natural building stone. *Geomech. Geophys. Geo-Energy Geo-Resour.* **2024**, *10*, 6. [CrossRef]
28. Ding, G.; Liu, J.; Wang, L.; Wu, Z.; Zhou, Z. Discussion on determination method of long-term strength of rock salt. *Energies* **2020**, *13*, 2460. [CrossRef]

29. Tarifard, A.; Török, Á.; Görög, P. Review of the creep constitutive models for rocks and the application of creep analysis in geomechanics. *Rock. Mech. Rock. Eng.* **2024**, *57*, 7727–7757. [CrossRef]
30. Tarifard, A.; Török, Á.; Görög, P. Fractional derivative-based Burger creep model for soft rocks and its verification using tunnel monitoring results and experimental data. *Arab. J. Sci. Eng.* **2025**, *50*, 16453–16464. [CrossRef]